ORIGINAL ARTICLE

A new crystal plasticity model incorporating precipitation strengthening to simulate tensile deformation behavior of AA2024 alloy

Lakhwinder Singh[1] · Sangyul Ha[2] · Sanjay Vohra[1] · Manu Sharma[1]

Abstract

In this work, a constitutive model is developed by incorporating precipitation strengthening into a dislocation-density-based crystal plasticity (CP) model to simulate the mechanical properties of 2024 aluminium alloy (AA). The proposed model considers the contributions of solid solution strengthening and strengthening from dislocation–precipitate interactions into the total slip resistance along with the forest hardening due to dislocation–dislocation interactions. A term accounting for the multiplication of dislocations due to their interactions with the non-shearable precipitates in the alloy is incorporated in the hardening law. The developed precipitation strengthening-based CP model is implemented into the crystal plasticity finite element method (CPFEM) for simulating the macroscopic mechanical behavior of AA2024-T3 alloy for uniaxial tension over various strain rates. The macroscopic response of the polycrystal representative volume element (RVE) used for simulations is computed using computational homogenization. The effect of meshing resolution on the RVE response is studied using four different mesh discretizations. Predictions of the macroscopic behavior by the developed model are in good agreement with the experimental findings. Additionally, the contribution of model parameters to the total uncertainty of the predicted stress has been assessed by conducting a sensitivity analysis. A parametric analysis with different precipitate radii and volume fractions has been done for finding the effect of precipitates on the macroscopic and localized deformation.

Keywords Precipitation hardening · Dislocations · Representative volume element · AA2024-T3 · Crystal plasticity

1 Introduction

Aluminium alloys (AA) have found widespread application in the aerospace and automotive sectors owing to their high strength-to-weight ratios along with other favorable properties [1]. The strength of these alloys derives from the precipitates that are intentionally grown by a proper heat treatment process within the aluminium (Al) matrix [2]. Such aluminium alloys are capable of competing with heavy materials like iron and steel owing to their use in many lightweight

and structural applications. AA2024 is an aluminium-copper-magnesium (Al-Cu-Mg) alloy with attractive properties for example high strength, damage tolerance and fracture toughness [1]. In T3 and T4 temper conditions, the sheets of AA2024 alloy are generally used for making aircraft wings and fuselage structures [3].

The high strength of these alloys arises from the hindrance to the motion of dislocations resulting from interactions of dislocations and precipitates. Based upon the size of the precipitates, the dislocations can interact with them in two ways: (a) either they can shear or cut through the precipitates or (b) they can bypass the precipitates to form Orowan loops around them [4]. Sehitoglu et al. [5] observed that the Guinier–Preston (GP) zones coherent with the aluminium matrix raise its yield strength whereas the strain hardening behavior is not much affected. Whereas, the non-shearable θ' and θ precipitates obstruct the movement of dislocations, hence, resulting in an increased work hardening. Similarly, Esin et al. [6] found that the precipitates in AA2024 alloy are formed by the nucleation out of Cu and Mg solutes as

✉ Lakhwinder Singh
  lakhwinder.fme@gmail.com

✉ Sangyul Ha
  dubuking@postech.ac.kr

1 Department of Mechanical Engineering, UIET Panjab University, Chandigarh 160014, India

2 PKG Development, SK Hynix, Icheon 17336, Republic of Korea

particles of size ranging from nm-μm during the heat treatment process. For Al-Cu-Mg alloys, only the precipitates of S (Al_2CuMg) phase are expected to be formed at the equilibrium state if $1.5 < Cu/Mg < 4$. However, S (Al_2CuMg) phase precipitates along with θ (Al_2Cu) phase should be formed at the equilibrium state for the alloys with $4 < Cu/Mg < 8$. In another study, García-Hernández et al. [7] reported that for AA2024 alloy, increased hardening is favored by small size, uniform spatial distribution and high number density of non-shearable S precipitates which provides effective locations for dislocation accumulation and trapping. Therefore, the S phase (non-shearable) precipitates are responsible for strengthening of the AA2024 alloys whose composition generally have Cu-Mg content in the ratio of $1.5 < Cu/Mg < 4$.

Crystal plasticity (CP) models are used for polycrystalline materials to study their deformation behavior by accounting for the underlying physical mechanisms which derive the constitutive response at the single crystal (or grain) level. The morphological properties of the material are also explicitly included in the CPFE model, allowing accurate predictions at both microscopic and macroscopic levels. Precipitation hardening effects have been incorporated into crystal plasticity frameworks by researchers in an effort to predict the deformation behavior of aluminium alloys. Sehitoglu et al. [5] updated the visco-plastic self-consistent (VPSC) model of Lebensohn and Tomé [8] by incorporating a new hardening formulation used by Acharya et. al [9] to study the response of pure aluminium and precipitate-hardenable Al-Cu alloy. The evolutionary equation for dislocation density was adjusted by incorporating the effect of precipitate spacing on the alloy's hardening behavior. Additionally, to consider the precipitate effect on anisotropy, a weighting function dependent on the orientation of grain, its morphology and the orientation of precipitates was incorporated into the hardening formulation. The experimental stress–strain behavior and precipitate effect on plastic anisotropy [10] were reasonably captured by their model. However, they did not demonstrate that their model could be used for a strain rate-based deformation study of Al-Cu alloy. In another work, Bhattacharyya et al. [11] used the framework of the elastic-plastic self-consistent (EPSC) single crystal model of Turner and Tome [12] to incorporate a hardening formulation for simulating the kinematic hardening effect on back-stress and anisotropy induced by precipitates for AA7085 alloy. However, they employed simplifications to obtain strain relaxation within the precipitate phase, elastic properties and morphology of the precipitates. Anjabin et al. [13] adopted the resistance due to precipitates from Myhr et al. [14] and Goutterbroze et al. [15] into crystal plasticity mechanics to analyse how precipitates influence the mechanical behavior of an Al-Mg-Si alloy. They considered the additional contributions to slip resistance due to precipitates and solutes for calculating the critical resolved

shear stress. Further, they also modified the standard dislocation evolution model of Kocks-Mecking-Estrin (KME) [16, 17] to consider the dependency of flow stress on precipitation strengthening. An additional term i.e. geometric storage distance was incorporated into the dislocation evolution equation which depends on the weighting function similar to Sehitoglu et al. [5], for considering the impact of non-shearable precipitates on the plastic anisotropy. However, important aspects like precipitate anisotropy or crystallographic texture were neglected.

Homogenization techniques in conjunction with CP models are effective for connecting the macroscopic response of the material to its microstructural state. Li et al. [18] modeled the precipitation strengthening with the yield model approach of Esmaeili et al. [19] and the interactions between the constituent phases of individual crystals were modelled using the mean-field homogenization approach of Molinari et al. [20]. It was validated for AA6060 alloy to study its mechanical response and precipitate anisotropy. Recently, Li et al. [21] followed the research of Bardel et al. [22] for modeling the strengthening due to dislocation-precipitate interactions and adopted the solid solution strengthening from Myhr et al. [14]. Additionally, they used the same elastic-viscoplastic (mean-field) homogenization scheme of Li et al. [18] to predict the deformation of AA6061 alloy. These studies, however, are limited to the application of mean-field homogenization techniques, and the capabilities of their models are not evaluated for the loading conditions at different strain rates.

The majority of studies on the prediction of AA2024 alloy deformation behavior rely on constitutive models that are phenomenological and do not account for the real microscopic mechanisms causing plastic deformation. On the other hand, physics-based constitutive models considering the actual mechanisms responsible for deformation are more reliable for achieving correct predictions. As a result, the material behavior can be more accurately predicted using CP models. Employing the flow rule of power law form [23], Li et al. [24, 25] simulated the AA2024 alloy's nano-indentation with the phenomenological CP model. Efthymiadis et al. [26], in a similar way, examined the AA2024 alloy's cyclic deformation using the same CP model aside from the incorporation of back-stress into the flow rule. These investigations, however, did not take into account periodic boundary conditions. Toursangsaraki et al. [27] also employed the phenomenological CP model to investigate the tensile deformation and high cycle fatigue of laser-peened AA2024-T351 alloy. In another study, Aghabalaeivahid et al. [28] investigated the influence of constituent phases on AA2024 alloy's tensile deformation using the phenomenological model of crystal plasticity with the flow rule of power law form and secant-hardening rule [29]. However, they used uniform displacement boundary conditions for the simulations. For AA2024 alloy, the literature on

CP modeling-based examinations of its deformation is also restricted to phenomenological constitutive descriptions and uniform displacement boundary conditions. In the literature, the study on the deformation behavior of AA2024 alloy with a dislocation density-based CP model incorporating precipitation strengthening is not available.

Therefore, the approach of this work is to propose a dislocation density-based model of crystal plasticity by considering the precipitation strengthening to predict the tensile deformation behavior of AA2024-T3 alloy. This model defines the slip resistance and hardening formulations accounting for the effect of precipitates on the strength and hardening rate of the alloy, respectively. The main objectives of this work are: (i) to propose a dislocation density-based CP model by incorporating the precipitate strengthening. As a result, the mechanical response of single grain is described by the developed constitutive model, and the macroscopic deformation response is obtained using a computational homogenization method based on the representative volume element (RVE) that depicts the synthetic microstructure of polycrystalline materials. The developed computational procedure is verified with the experimental results of the AA2024-T3 alloy for different strain rates. Additionally, (ii) a mesh sensitivity study with four different meshing resolutions is conducted to investigate their influence on RVE behavior. (iii) Further, the uncertainty contributed by the CP parameters to the mechanical response from the CP simulations is quantified by sensitivity analysis. (iv) An exploratory study is also carried out to examine the response of the alloy for the distribution and size of the precipitates.

The following is the outline for this paper: Sect. 2 explains the constitutive model incorporating the effect of precipitates in the crystal plasticity framework. Section 3 briefs the periodic boundary conditions and computational homogenization employed to compute the RVE's macroscopic response. Section 4 discusses the details of RVE used for performing CP simulations. Section 5 describes the calibration of the model parameters and validation of simulation findings against the experimental data. A sensitivity analysis detailing the extent to which variations in the model parameters contributed to the overall uncertainty in the predicted stress is also provided. Additionally, this section discusses the deformation behavior of material for variation in precipitate size and volume fraction followed by the conclusions in Sect. 6.

2 Bridging the precipitation strengthening with CP constitutive model

2.1 CP model for single crystal

A CP model based on dislocation density is used here as a foundation to implement the effect of precipitates into the constitutive law of a single crystal. In the following subsections, the deformation kinetics of a single crystal incorporating the solid solution and precipitation strengthening is presented followed by the substructure evolution part of the CP model. The details on the kinematics and kinetics employed for the single crystal deformation are described in Appendix A.1 and A.2 respectively.

2.2 Kinetics

On a slip system α, the rate of plastic shearing is defined as [30]:

$$\dot{\gamma}^{\alpha} = \dot{\gamma}_0 \exp\left[-\frac{F_0}{k_B \theta}\left\{1 - \left\langle \frac{|\tau^{\alpha}| - \tau_a^{\alpha}}{\hat{\tau}_o \frac{\mu}{\mu_0}} \right\rangle^p\right\}^q\right] sgn(\tau^{\alpha}) \quad (1)$$

where the symbol $\dot{\gamma}_0$ stands in for the reference slip rate. F_0 stands for the Helmholtz free energy of activation, k_B represents the Boltzmann constant and θ is the temperature. $\hat{\tau}$ denotes the strength which is overcome by the dislocations without any aid of thermal activation and $\hat{\tau}_o$ is its value at 0 K. At temperatures θ and 0 K, the shear moduli of material are denoted by μ and μ_0 respectively. The resolved shear stress is denoted by τ^{α} and τ_a^{α} represents the athermal slip resistance. $\langle \rangle$ represents the Macaulay bracket such that $\langle x \rangle (:= [|x| + x]/2)$. The energy-barrier profile associated with dislocation-obstacle interactions is determined by the parameters p and q.

$$0 \leq p \leq 1 \quad \text{and} \quad 0 \leq q \leq 2 \quad (2)$$

By incorporating the solid solution and precipitation strengthening contributions, the total athermal slip resistance is expressed as:

$$\tau_a^{\alpha} = \tau_d^{\alpha} + \tau_{ss}^{\alpha} + \tau_p^{\alpha} \quad (3)$$

where τ_d^{α} is the hardening contribution from dislocation-dislocation interactions, τ_{ss}^{α} denotes the contribution of solid solution strengthening and τ_p^{α} is the precipitation strengthening arising from dislocation-precipitate interactions.

The contribution due to dislocation-dislocation interactions is expressed by the Taylor law of hardening [30–32] as,

$$\tau_d^{\alpha} = \lambda \mu b \sqrt{\sum_{\beta=1}^{N} h^{\alpha\beta} \rho_T^{\beta}} \quad (4)$$

where the statistical coefficient λ accounts for the irregularity in the spatial distribution of dislocation densities and b denotes the magnitude of the Burgers vector. The interaction matrix $h^{\alpha\beta}$ captures the rate at which the slip resistance of system α increases as a result of shearing on system β. In the current work, the following simple form of $h^{\alpha\beta}$ is adopted.

$$h^{\alpha\beta} = \omega_1 + (1 - \omega_2)\delta^{\alpha\beta} \tag{5}$$

where ω_1 and ω_2 represent the interaction coefficients and $\delta^{\alpha\beta}$ signifies the Kronecker delta.

Due to the solutes present in the aluminium matrix, the solid solution strengthening contribution is expressed in terms of concentrations of the solutes [14]:

$$\tau_{ss}^{\alpha} = \sum_i k_i C_i^{\frac{2}{3}} \tag{6}$$

where for the ith solute, C_i denotes its concentration and k_i is the corresponding scaling factor. Here, only the primary solutes Cu and Mg are considered and their concentrations used corresponding to the experimental data [33] are 4.3 wt% and 1.5 wt% respectively.

The strengthening due to dislocation-precipitate interactions results from the reduction in dislocation mean-free path owing to the presence of precipitates in the alloy. Depending upon the precipitate size, the dislocations can interact with the precipitates in two ways: either the dislocations can shear the precipitates or bypass them. The current model employs the approach of Khan et. al [34] for modeling the strengthening contribution from the S phase rod-shaped, non-shearable precipitates in AA2024 alloy. This strengthening based on the mechanism of Orowan looping due to the rod-shaped, non-shearable S phase precipitates is expressed as:

$$\tau_p^{\alpha} = \frac{0.075\mu b}{r_p} ln\left(\frac{2.632 r_p}{r_0}\right)\left(\sqrt{f_p} + 1.84 f_p + 1.84 f_p^{\frac{3}{2}}\right) \tag{7}$$

where r_p is the average radius of non-shearable S phase precipitates and f_p is the precipitate volume fraction. The calculation of dislocation line tension requires an inner cutoff radius which is denoted by r_0.

2.3 Substructure evolution

During plastic deformation, to obtain an accurate material response, it is important to propose the appropriate equations for the dislocation substructure's evolution. At a material point, the total dislocation density affects the evolution of the athermal slip resistance. The total statistically stored dislocation density ρ_T^{α} is divided into edge ρ_e^{α} and screw ρ_s^{α} components.

$$\rho_T^{\alpha} = \rho_e^{\alpha} + \rho_s^{\alpha} \tag{8}$$

At room temperature and on a macroscopic scale, two physical processes i.e. storage and recovery control the evolution of dislocation densities. These processes rely on the dislocations moving slowly through the crystal. The storage process results from the multiplication of dislocations from discrete sources like the Frank-Read source. Whereas, the recovery

process is associated with the annihilation from the edge dislocations with opposite polarity, and the annihilation from the cross slip of screw dislocations. The S phase non-shearable precipitates in AA2024 alloy obstructing dislocation movement will lead to the dislocation accumulation around the precipitates in the form of Orowan loops. Therefore, to account for these accumulations of dislocations due to the reduction in dislocation mean-free path and its effect on the hardening rate, the dislocation density evolution equations are formulated by including a new term based on research by Bardel et. al [35]. On a slip system α, the evolutionary equations for edge and screw components of dislocation density are defined as:

$$\dot{\rho}_e^{\alpha} = \frac{C_e}{b}\left[K_e\sqrt{\sum_{\beta=1}^{N}\rho_T^{\beta}} + \frac{\phi}{r_p}\sqrt{\frac{f_p}{2\pi}} - 2d_e\rho_e^{\alpha}\right]|\dot{\gamma}^{\alpha}| \tag{9}$$

$$\dot{\rho}_s^{\alpha} = \frac{C_s}{b}\left[K_s\sqrt{\sum_{\beta=1}^{N}\rho_T^{\beta}} + \frac{\phi}{r_p}\sqrt{\frac{f_p}{2\pi}} - \rho_s^{\alpha}\left\{K_s\pi d_s^2\sum_{\beta=1}^{N}\rho_T^{\beta} + 2d_s\right\}\right]|\dot{\gamma}^{\alpha}| \tag{10}$$

where C_e is the contribution of edge dislocation segments to the total slip rate and C_s is the contribution of screw dislocation segments. The dimensionless proportionality constants K_e and K_s control the dislocation mobility. d_e and d_s are the maximum distances for mutual annihilation to take place between anti-parallel edge and screw components and thus are linked with the dislocation recovery processes. Additionally, the term ϕ in the above equations denotes the storage efficiency for trapped dislocations such that $0 \leq \phi \leq 1$. For the current work, the value of ϕ is taken as unity [35]. The above CP model is implemented through a subroutine UMAT in ABAQUS and the time integration procedure used for the same is mentioned in Appendix A.3.

3 Computational homogenization

In polycrystalline materials, every (macroscopic) material point is made up of several grains or single crystals with various shapes and orientations. Therefore, the overall response of the material point is determined by the sum of the responses of the individual single crystals comprising it. The polycrystalline or macroscopic response is computed from the single crystal (or microscopic) response through homogenization techniques. In computational homogenization, the boundary value problem at the microscopic level is numerically solved and the macroscopic fields are computed by volume averaging the microscopic fields [36–38]. The basis for computational homogenization in this study is the numerical solution of the following governing equation with a crystal plasticity finite element (FE) model.

$$\nabla \cdot \boldsymbol{\sigma} = 0 \tag{11}$$

By volume averaging, the stress at a macroscopic material point is computed as follows:

$$\overline{\boldsymbol{\sigma}} = \frac{1}{V} \int \boldsymbol{\sigma} dV = \frac{\sum_{j=1}^{N} \sigma^j V^j}{\sum_{j=1}^{N} V^j} \tag{12}$$

where N represents the total number of integration points. The volume connected with the jth quadrature point is denoted by V^j which corresponds to the product of the weight of the corresponding point within the element and the volume of that element.

3.1 Periodic boundary conditions

Even under uniform macroscopic external force, an anisotropic material may nonetheless experience non-uniform deformation. Application of periodic boundary conditions in place of uniform displacement or force boundary conditions can result in more accurate estimations of the effective behavior of RVE, as demonstrated by previous studies [39–41]. Therefore, in the current work, periodic boundary conditions are employed for the RVE. Under the periodic boundary conditions, it is assumed that the entire RVE deforms like a jigsaw puzzle and it is periodically translated along the three coordinate axes to fill the full space. To apply the periodic boundary conditions in the finite element simulations, the displacement of every pair of parallel and opposite cube faces is connected by multipoint constraints [36–38]. Appendix A.4 describes the periodicity boundary condition to be satisfied by the cubic RVE.

In practice, for two parallel and opposite surfaces of RVE, the displacement fields are subtracted from each other to apply the multiple-point kinematic constraints.

$$\mathbf{u}(N_k^+) - \mathbf{u}(N_k^-) = (\overline{\mathbf{F}} - \mathbf{I})\mathbf{L}_k = \mathbf{u}(M_k)(k = 1, 2, 3) \tag{13}$$

For the cubic RVE, the displacement of N_k^+ node on the surface S^+ is shown here by the symbol $\mathbf{u}(N_k^+)$ and the displacement of its matching N_k^- node located on the parallel opposite surface S^- is represented by $\mathbf{u}(N_k^-)$. The vector $\mathbf{L}_k$ represents the length along the axis x_k. A master node M_k is defined for each set of opposing faces of the RVE, and its displacement is indicated by the notation $\mathbf{u}(M_k)$. In this work, the implementation of periodic boundary conditions is done through a Python script which first identifies the corresponding nodes on a pair of parallel opposite surfaces and then using Eq. (13) their degrees of freedom are constrained. A detailed description of the constraint equations used for applying periodic boundary conditions may be found in the reference [42].

4 Model implementation

The AA2024-T3 aluminium alloy has been used to apply the constitutive relations. Since experimental data at the various deformation rates is available for AA2024-T3 alloy, we have opted to simulate its behavior with the proposed CP model. Additionally, applications pertaining to the aerospace and automotive industries need a good understanding of its deformation behavior.

4.1 Simulation details

The truncated octahedron-based RVE, which employs a truncated octahedron to represent the shape of a grain, can more realistically depict the microstructure of polycrystalline materials [43]. However, when compared to the other RVE models, its computing time is unnecessarily high [37]. This investigation is therefore carried out using the grain-based RVE model which discretizes every single grain into several cubic elements.

The precipitation strengthening-based CP model has been implemented through a UMAT subroutine in ABAQUS using C3D8R (Three-dimensional eight-noded element with reduced integration) elements. Recent research has demonstrated that the local micromechanical fields, especially those near the grain boundaries are affected by the type of element employed in CPFE investigations [44, 45]. They have concluded that in comparison to linear tetrahedral and quadratic hexahedral elements, the quadratic tetrahedral and linear hexahedral elements are more accurate. A synthetic RVE with 200 grains, having random orientations and discretized by hexahedral finite elements, has been generated through open-source software Neper [46] to represent the alloy's microstructure. Former investigations have reported that to obtain the homogenized results, an RVE of 200 grains is adequate [47]. Every grain is sub-discretized into multiple elements (Fig. 1(a)) and the different colors therein stand for the different grain orientations. In nature, the grains are equiaxed and have random orientations as described by the pole figure (Fig. 1(b)). The open-source package ATEX [48] has been used to plot the pole figure. In Neper, the grains are generated through tessellation with a normal distribution of grain size (Fig. 1(c))) having a mean value of 19 μm. The Gmsh package has been used to mesh them into hexahedral finite elements. The references [46, 49] provide detailed information regarding the creation and meshing of polycrystals using Neper.

(a)

(b)

(c)
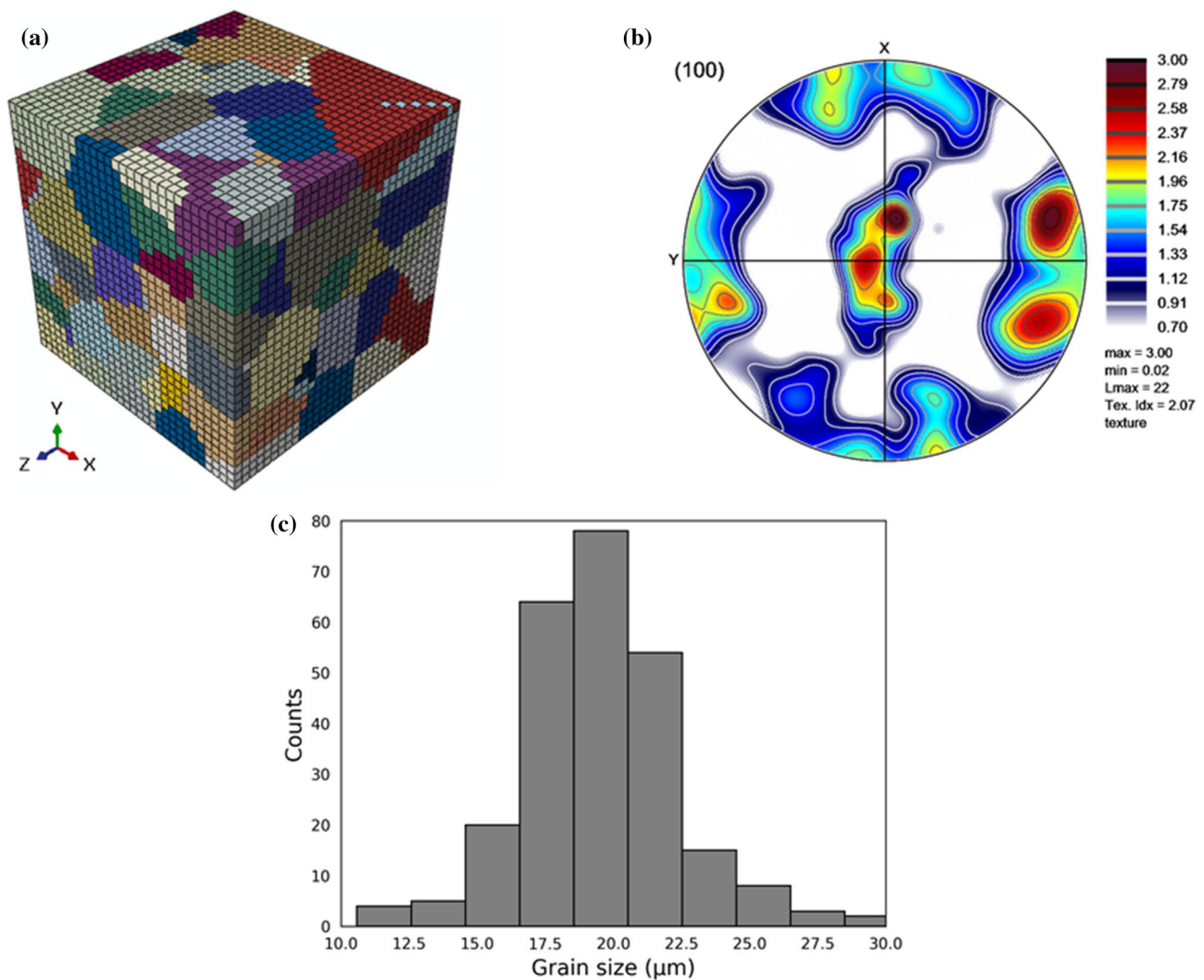
Fig. 1 **a** RVE of 200 grains and discretized by 40^3 elements, **b** a pole figure corresponding to orientations of grains and **c** a normal distribution assumed for grain size to generate the RVE

5 Results and discussions

Results from an investigation of tensile deformation in AA2024-T3 aluminium alloy are reported in this section. The stress–strain responses attained in experiments [33] have been simulated through the proposed model of crystal plasticity. Additionally, the deformation behavior of the alloy has been investigated for the variations in volume fraction and size of precipitates.

5.1 Material parameters identification

The material parameters have been identified by calibrating the macroscopic response of the CP model with the experimental curves. The parameters of the flow and hardening laws of the proposed CP model were adjusted to fit

the macroscopic response curves of AA2024-T3 alloy over the different strain rates. The set of parameters used by Ha et. al [50] for pure aluminium was taken as an initial set to start the fitting procedure. The parameters C_e and C_s were set equal to 0.5 by assuming an equal slip contribution from the edge and screw dislocations. Additionally, the value of parameter d_s was taken as five times of d_e, i.e. $d_s = 5d_e$ and K_s was set as twice of K_e, i.e. $K_s = 2K_e$ [31, 51].

To determine the material parameters, initially, a parametric study was done to find the effect of every CP model parameter on the predicted response curve. A rise in the yield stress was observed by increasing the value of flow parameters F_0, $\hat{\tau}_0$, p, and decreasing the value of parameter q. Similarly by increasing the value of scaling factors k_{Cu} and k_{Mg} corresponding to the concentrations of Cu and Mg in the solid solution, an increase in the yield stress was

found. Further, by increasing the hardening parameters K_e and d_e, an increase in the hardening rate and saturation stress was noted. After identifying these model parameters which significantly affect the flow stress and hardening rate, their values were adjusted through multiple simulations to match the experimental curves. Table 1 contains the values of CP model parameters determined from the simulation-based fitting of the experimental curves of alloy AA2024-T3. The values of parameters k_{Cu} and k_{Mg} have been identified from the simulations. For Al-Cu-Mg alloys, the value of the inner

cut-off radius, r_0, has been taken from the reference [52]. Additionally, the range for the precipitate radius and volume fraction for performing the CP simulations has been decided from the references [18, 52].
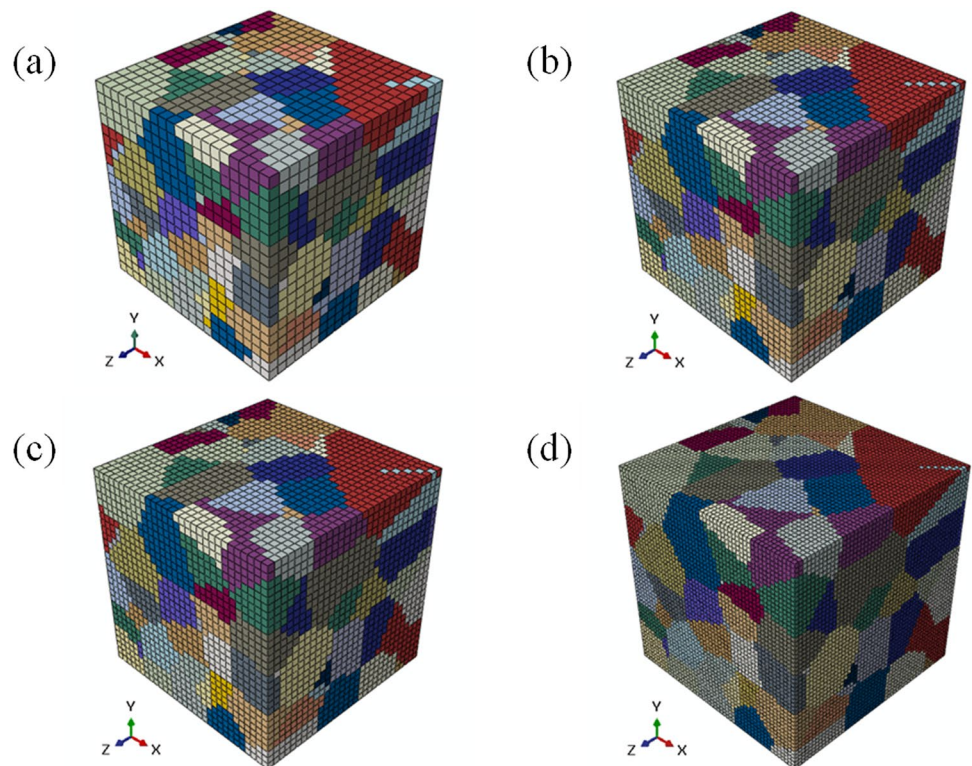
RVEs with four different mesh resolutions of 20^3, 30^3, 40^3 and 50^3 comprising of a total of 8000, 27000, 64000 and 125000 finite elements respectively as shown in Fig. 2, were created with 200 grains and all the RVEs had the same set of orientations. Using the identified CP model parameters listed in Table 1, the simulations under a 10% uniaxial tensile strain at 0.001 and 10 s^{-1} were performed to determine the effect of the meshing resolution. The corresponding curves of the stress–strain responses of the RVEs with different mesh resolutions are shown in Fig. 3(a) and 3(b). It is evident from the plot that the difference between the responses of meshing resolutions of 40^3 and 50^3 is very small, hence, the mesh resolution of 40^3 was chosen for the simulations to reduce the computational cost. Further, Fig. 3(c) and (d) depicts the equivalent plastic strain plots for RVEs with 20^3 and 50^3 elements respectively, simulated at 0.001 s^{-1}. The latter has a more diffusive nature of the shear bands and this results in the slightly lower stress level shown in Fig. 3(a).

CP simulations were performed at various strain rates under uniaxial tension for AA2024-T3 alloy with the RVE of 200 grains having random orientations and discretized by a regular mesh of 40^3. The CP simulation curves, as seen in Fig. 4, match the experimental ones [33] previously reported for the same alloy. The slope of the strain hardening portion

Table 1 Identified CP model parameters

Parameter	Magnitude	Parameter	Magnitude
$\dot{\gamma}_0$	$1.73 \times 10^6 \, s^{-1}$	d_e	0.07 nm
F_0	185 kJ	d_s	0.35 nm
$\hat{\tau}_o$	65 MPa	μ	25 GPa
p	0.28	μ_0	28 GPa
q	1.16	ω_1	1.5
K_e	22.9×10^{-3}	ω_2	1.2
K_s	45.8×10^{-3}	λ	0.3
C_e	0.5	b	0.286 nm
C_s	0.5	r_0	0.572 nm
k_{Cu}	17.5 MPa/$Wt\%^{\frac{2}{3}}$	r_p	1.78 nm
k_{Mg}	8.0 MPa/$Wt\%^{\frac{2}{3}}$	f_p	0.5 %
ϕ	1		

Fig. 2 RVEs with 200 grains having mesh discretizations of **a** 20^3, **b** 30^3, **c** 40^3 and **d** 50^3 C3D8R elements
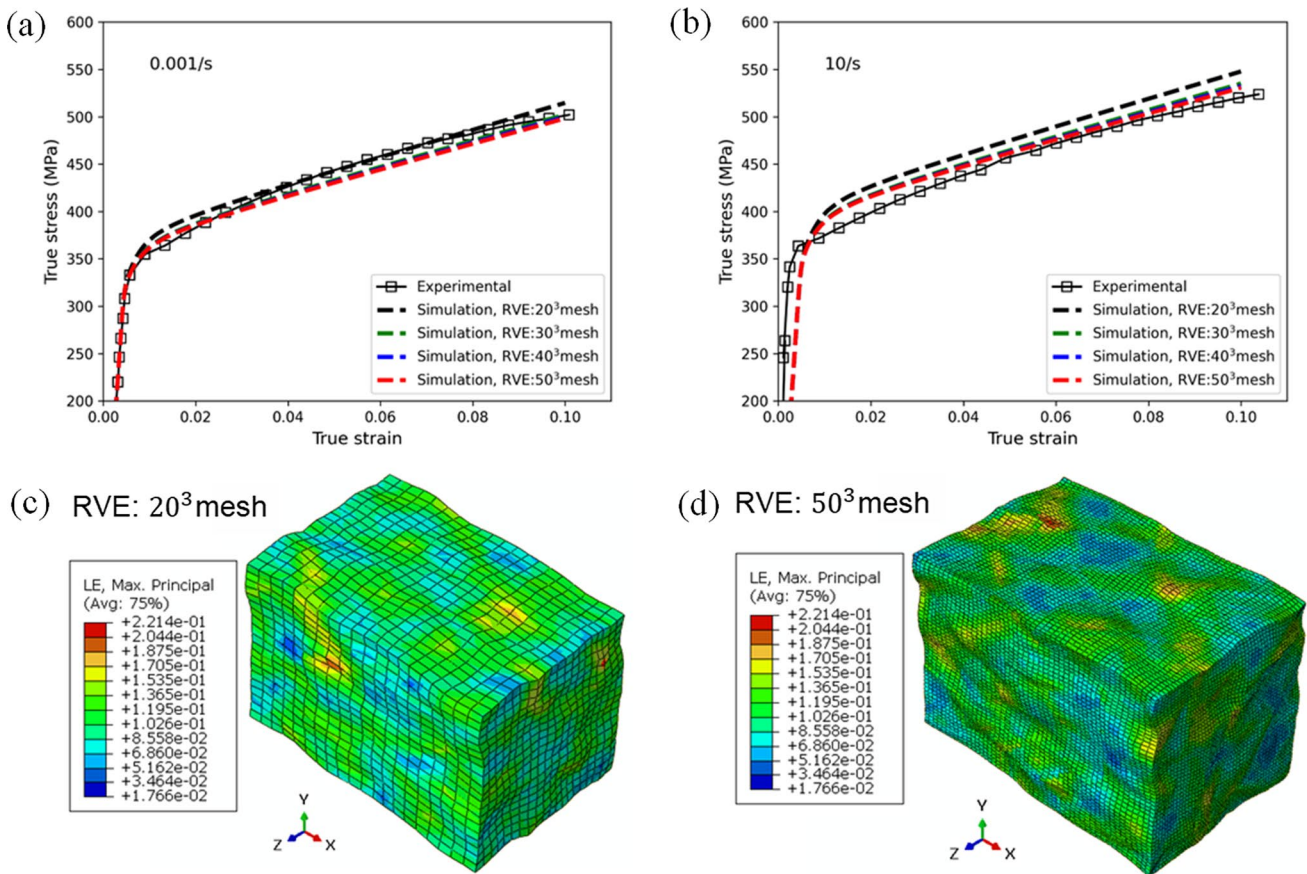
Fig. 3 Stress–strain response curves at strain rates of **a** 0.001 s^{-1}, **b** 10 s^{-1} and **c,d** distributions of maximum principal strain at 0.001 s^{-1} for RVEs with different mesh resolutions

of the simulated curves is almost similar to the experimental curves at all the strain rates. At higher strain rates of 10 and 100 s^{-1} (Fig. 4(c) and (d)), higher yield stress as compared to 0.001 and 0.01 s^{-1} (Fig. 4(a) and (b)) has been well predicted by the CP model. It is clear from Fig. 4(a) to (d), that the material's ability to withstand strain does not diminish as the strain rate rises. The comparatively modest and almost linear strain rate sensitivity as observed in experimental results has been successfully captured by the CP model.

5.2 Sensitivity analysis

The model parameters for AA2024-T3 alloy are calibrated against macroscopic experimental data for its uniaxial tension over various strain rates. Sensitivity analysis has been performed through the FOSM (First Order Second Moment) technique [53] to quantify uncertainty in the mechanical response from CP simulations. Let $\phi(\mathbf{y})$ represent the output from the CPFE simulations having a scalar value, which is taken as the macroscopic stress (obtained from computational homogenization of the RVE response) in the loading direction for this analysis. Here, the CP model parameters are contained

in the vector $\mathbf{y}$. The mean of $\phi(\mathbf{y})$, i.e. $\bar{\phi}$, is determined via the FOSM technique as:

$$\bar{\phi} = \phi(\bar{\mathbf{y}}) \tag{14}$$

where the mean value of $\mathbf{y}$ is denoted by $\bar{\mathbf{y}}$ and V_ϕ i.e. the variance of $\phi(\mathbf{y})$ is given by:

$$V_\phi = \nabla\phi^T(\bar{\mathbf{y}})\mathbf{S}\nabla\phi(\bar{\mathbf{y}}) \tag{15}$$

where the $\nabla(\cdot)$ operator denotes the scalar's gradient with respect to $\mathbf{y}$ and $\mathbf{S}$ denotes the covariance matrix of $\mathbf{y}$. If the CP parameters, represented by $\mathbf{y}$, are independent of one another, $\mathbf{S}$ will change into a diagonal matrix in which the variance of individual CP parameters is represented by the diagonal elements. This allows us to determine how much uncertainty is added by an individual CP parameter to the overall uncertainty of $\phi(\mathbf{y})$, denoted by V_ϕ.

$$c_i^\phi = \frac{\left[\left|\left.\frac{\partial\phi(\mathbf{y})}{\partial y_i}\right|_{\mathbf{y}=\bar{\mathbf{y}}}\right|\right]^2 V_{y_i}}{V_\phi} \times 100\% \tag{16}$$
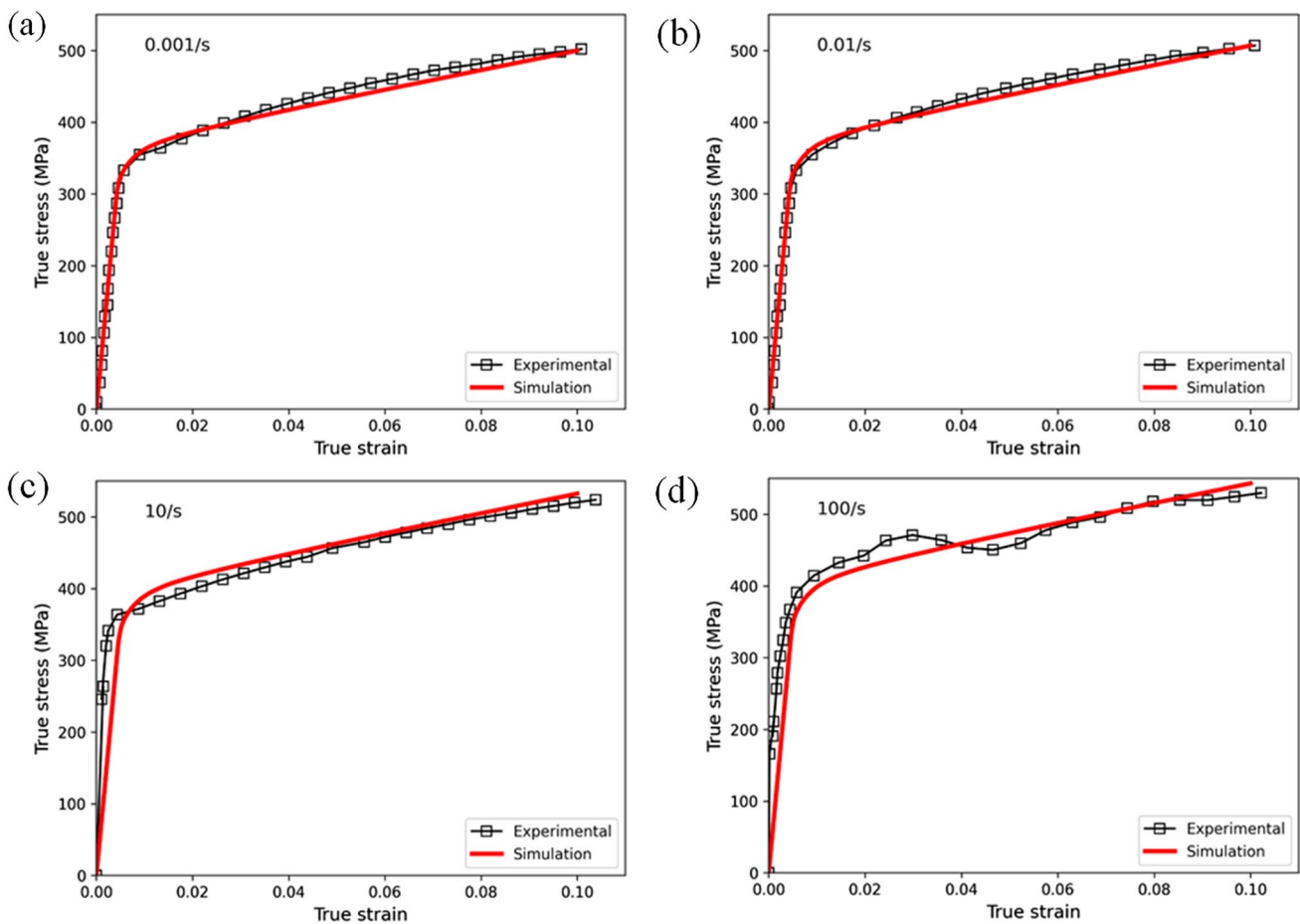
Fig. 4 Comparison of CP model predictions with the experimental results [33] over various strain rates

where c_i^ϕ is the ith CP parameter's variance contribution to $\phi(\mathbf{y})$ and V_{y_i} is the ith CP parameter's variance.

Using the results of the CPFE simulation, a central difference approach is employed to numerically obtain the gradient terms as:

$$\left|\frac{\partial\phi(\mathbf{y})}{\partial y_i}\right|_{\mathbf{y}=\bar{\mathbf{y}}} \approx \frac{\phi(\bar{\mathbf{y}}+\epsilon\bar{y}_i\mathbf{e}_i)-\phi(\bar{\mathbf{y}}-\epsilon\bar{y}_i\mathbf{e}_i)}{2\epsilon\bar{y}_i} \quad (17)$$

where ϵ is the perturbation in y_i such that $0 < \epsilon \leq 1$ and the ith column of the identity matrix, which has the same number of rows and columns as vector $\mathbf{y}$, is denoted by $\mathbf{e}_i$. ϵ is taken to be 0.1 in the current work. Therefore, V_ϕ and c_i^ϕ are determined according to Eqs. (15) and (16) utilizing the $\bar{\mathbf{y}}$ vector, $\nabla\phi(\bar{\mathbf{y}})$ vector and the $\mathbf{S}$ matrix from the CPFE simulations.

As discussed in Sect. 5.1, the parameters of the flow and hardening rules affect the yield stress and hardening portion's slope of the predicted curve. Therefore, seven flow and hardening parameters were chosen to perform the sensitivity analysis for gaining a clear understanding of their

contribution to the overall uncertainty in the macroscopic predicted stress. A 10% perturbation was made to each of the six material parameters (i.e. ϵ is taken to be 0.1). The sensitivity analysis has been performed for 10% uniaxial tension at 0.001 s^{-1}. Figure 5 illustrates the individual contribution of parameters to the variance, or overall uncertainty, of the predicted stress at various points along the curve. Along the stress–strain curve, it is clear that the CP parameters have an unequal contribution to the overall uncertainty of the predicted stress. The parameters $\dot{\gamma}_0$ and d_e have a negligible contribution to the overall uncertainty of stress. Figure 5(a) marks the points of interest on the response curve for estimating the contribution of parameters individually to the overall uncertainty of the predicted stress. The flow rule parameter q determines the form of the energy-barrier profile resulting from dislocation-obstacle interactions. Since near the yielding, a higher slip resistance due to dislocation-obstacle interactions is expected, therefore a higher contribution of parameter q to the total uncertainty is observed before and at the yield point as clear from Fig. 5(b) and (c). After the yield point, the hardening portion of the
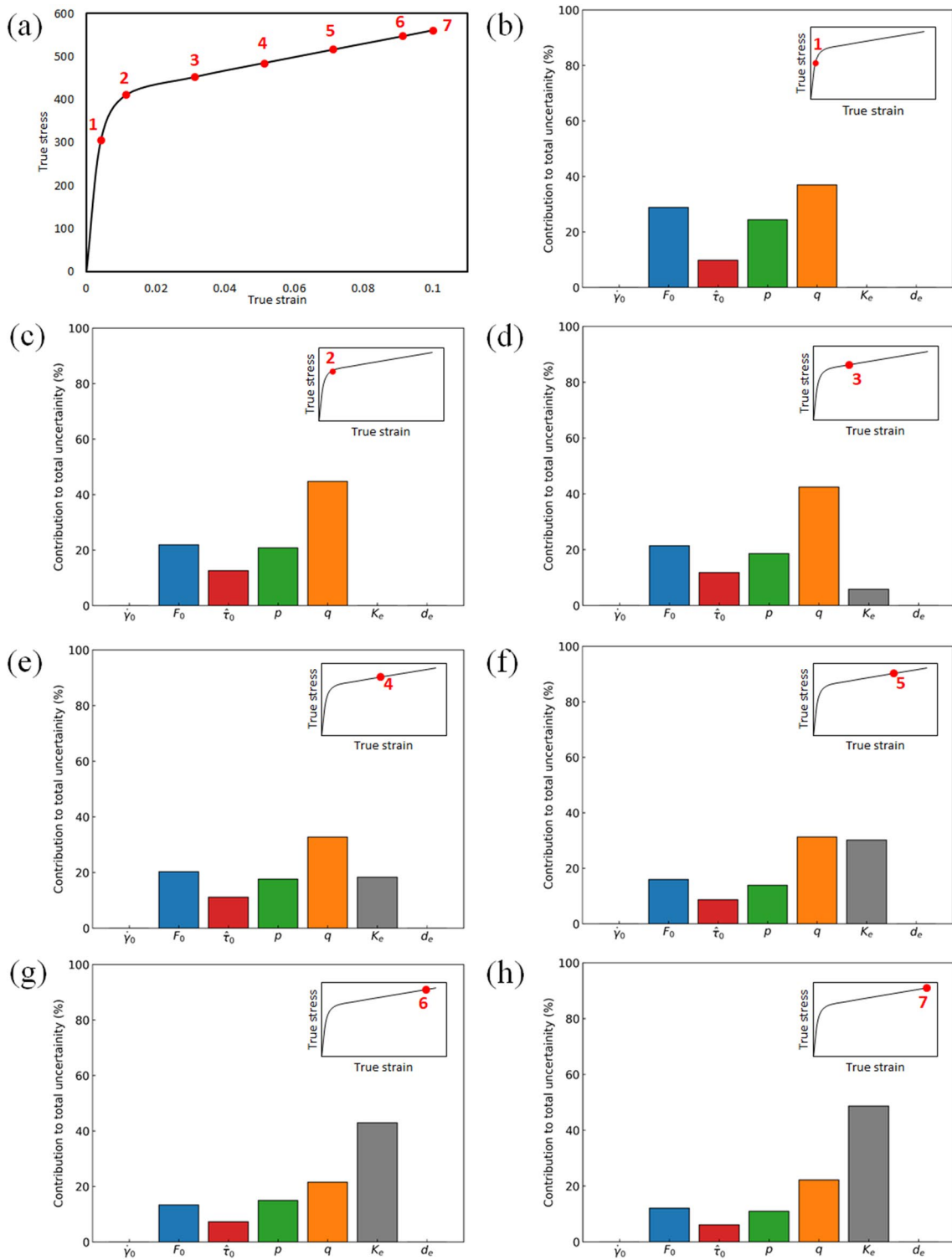
Fig. 5 Percentage of the overall uncertainty in the predicted stress that is caused by the CP model parameters with **a** the points of interest and **b**–**h** the corresponding loading points shown in the inset

curve is controlled by the interactions between dislocations resulting in the hardening of the material. The parameter K_e is associated with edge dislocation density's evolution and controls the mobility of dislocations. The contribution of K_e to the total uncertainty started rising (Fig. 5(d) and (e)) till it comes closer to the contribution of q as visible in

Fig. 5(f). Thereafter, the contribution of the parameter K_e dominates the other parameters, as visible in Fig. 5(g), and (h), which can be attributed to the linearly increasing rate of strain hardening as visible from the rising slope of the curve along these points.

5.3 Effect of radius and volume fraction of precipitates

Simulations have been performed for uniaxial tension of 10% along the x-axis at 0.001 s^{-1} to demonstrate the model's ability in capturing the effect of precipitate radius and volume fraction on local and macroscopic deformation. In Fig. 6, the macroscopic curves of stress–strain and slip resistance for different radii and volume fractions of precipitates are plotted.

To find the effect of precipitates on dislocation movement, the dislocation density's evolution is investigated for three different volume fractions of precipitates i.e. 0.5%,

1% and 2% at 1.78 nm average precipitate radius. Mechanical response of the RVE is predicted in the next set of simulations by considering three different precipitate radii i.e. 1.78 nm, 3.5 nm and 5 nm for 0.5% precipitate volume fraction. The contours of edge dislocation densities on the slip system ($\bar{1}$ 1 1) [1 1 0] for different volume fractions and radii are shown in Fig. 7. At higher precipitate volume fractions (Fig. 7(a) to (c)) and lower radii (Fig. 7(d) to (f)), there is an increase in the magnitude of the dislocation densities. This is also consistent with the physical phenomenon happening at the microstructure level. The S phase non-shearable precipitates result in the formation of Orowan loops around them [34], which increases the dislocations and resulting an increase in the slip resistance (Fig. 6(c) and (d)). This results in increased flow stress needed to propagate the slip which has also been well captured by the proposed CP model in terms of raised yield stress as evident from macroscopic response curves in Fig. 6(a) and (b).
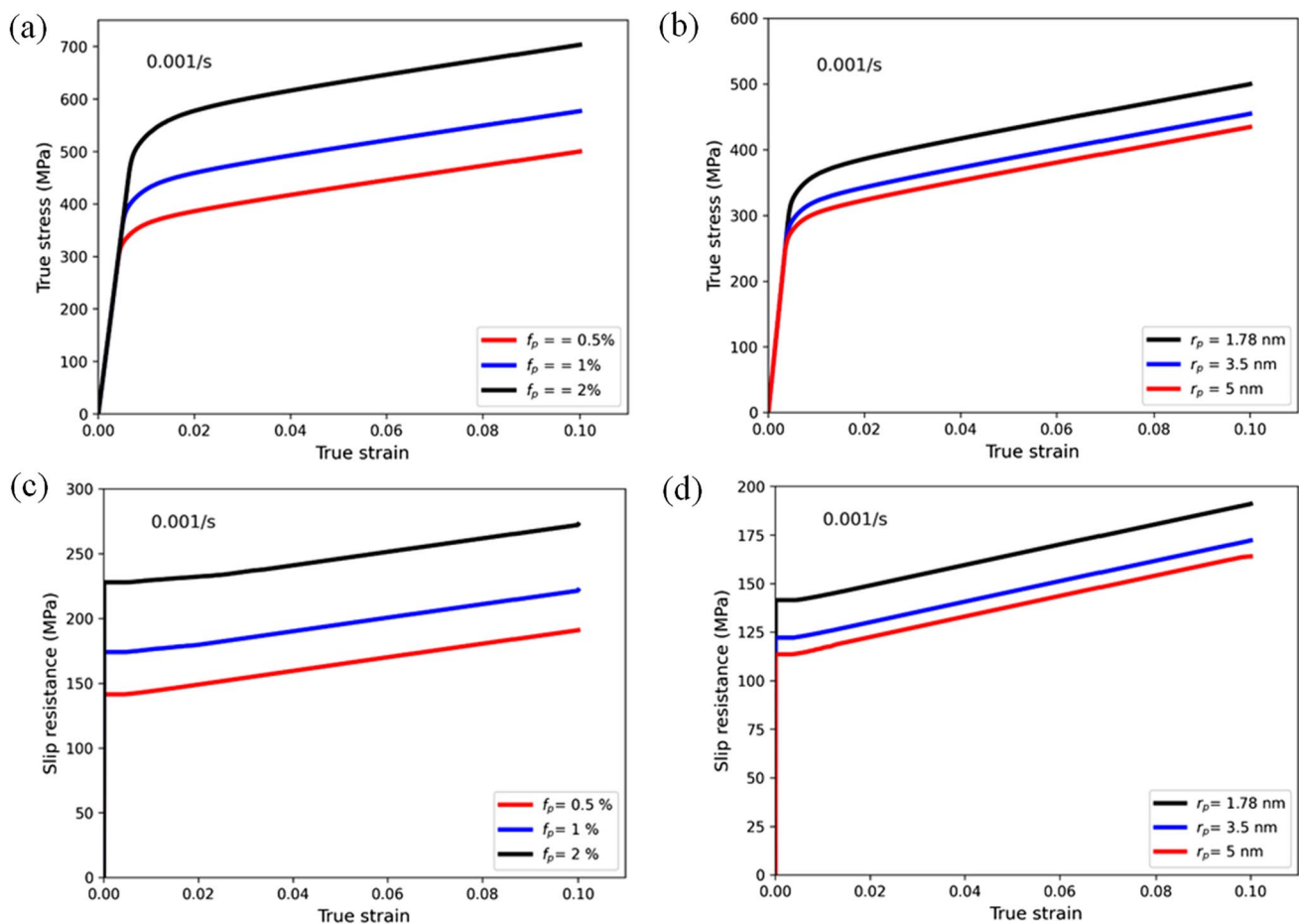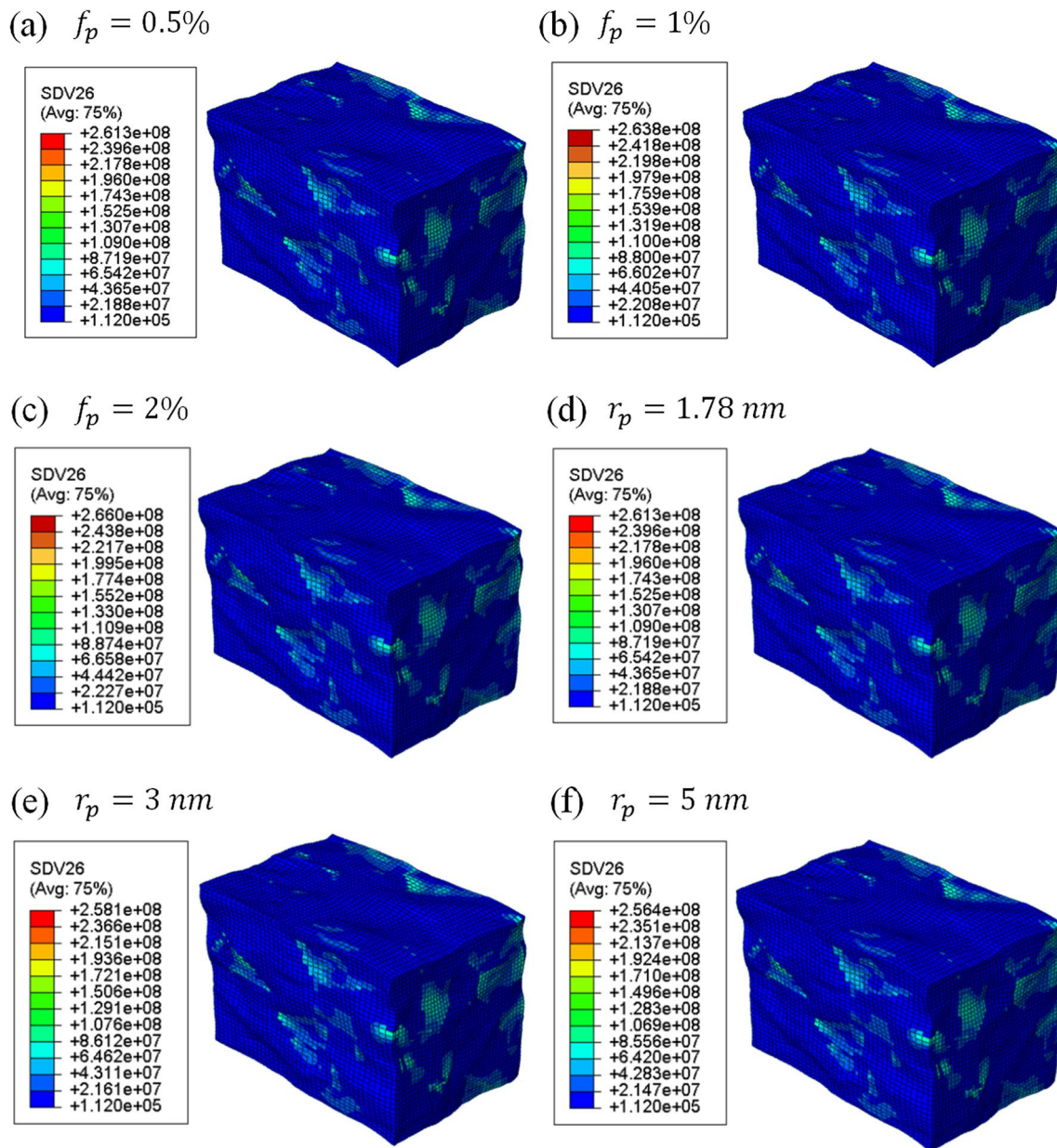

Fig. 6 Influence of precipitate **a**, **c** volume fraction and **b**, **d** radius on the macroscopic **a**, **b** stress and **c**, **d** slip resistance

(a) $f_p = 0.5\%$ (b) $f_p = 1\%$

(c) $f_p = 2\%$ (d) $r_p = 1.78\ nm$

(e) $r_p = 3\ nm$ (f) $r_p = 5\ nm$

Fig. 7 Contour plots of edge dislocation densities for precipitate volume fractions and radii on slip system ($\bar{1}\ 1\ 1$) [1 1 0]

6 Conclusions

To take into consideration precipitation strengthening in aluminium alloys, a new CP model has been proposed in the current work for usage within a finite element framework. The precipitation strengthening is taken into account by means of a precipitate-dislocation yield model and computational homogenization is employed for computing AA2024-T3 alloy's macroscopic response. The framework can be simply extended to other aluminium alloys that have similar non-shearable rod-shaped precipitates. A UMAT subroutine is written in FORTRAN to incorporate the proposed CP

model in the commercial FE package ABAQUS. Additionally, a sensitivity analysis for assessing the contribution of model parameters to the overall uncertainty of the predicted stress has been performed. A parametric analysis with different precipitate radii and volume fractions was conducted to examine their effect on the localized and macroscopic deformation. The important findings of the current study include:

- The proposed microstructure-based CP model is efficient in predicting the AA2024-T3 alloy's macroscopic behavior at various strain rates with only one set of model parameters. The RVE's macroscopic mechanical

response is examined for the influence of meshing resolution by considering four different mesh discretizations, based upon which the effective meshing size for the RVE has been used for the simulations.

- From the parametric study it is observed for the simulated curves that: (i) the strain rate dependency is captured by the flow parameters F_0, p, and q, while (ii) the parameters K_e and d_e affect the hardening rate and influence the curve shape between the yield and saturation stress points.

- Further, the uncertainty in the predicted stress has also been quantified by performing a sensitivity analysis for the CP model parameters. Consistent with the physics of deformation, it has been found that the individual contribution of CP model parameters to the overall uncertainty of predicted stress varies with the location of the point being investigated on the curve.

- To illustrate the strength of the proposed model, a parametric analysis has been conducted by varying the precipitate radius and volume fraction. For the higher volume fractions, a notable increase in both yield stress and slip resistance has been observed, whereas, they lower down for the higher precipitate radii.

An effort has been made to show the proposed model's strength and applicability, even though only a small parametric study has been attempted. For future investigations on precipitation-hardenable aluminium alloys, the proposed model provides a reliable physics-based basis.

Appendix

A.1 Kinematics

The deformation gradient, $\mathbf{F}$ is split into two parts as follows [29, 31, 54]:

$$\mathbf{F} = \mathbf{F}^e \mathbf{F}^p \tag{A.1}$$

where the respective elastic and plastic components of $\mathbf{F}$ are denoted by $\mathbf{F}^e$ and $\mathbf{F}^p$ such that $\det\mathbf{F}^e > 0$ and $\det\mathbf{F}^p = 1$. Using Eq. (A.1), the velocity gradient tensor $\mathbf{L}$ is decomposed as:

$$\mathbf{L} = \dot{\mathbf{F}}\mathbf{F}^{-1} = \dot{\mathbf{F}}^e\mathbf{F}^{e^{-1}} + \mathbf{F}^e\dot{\mathbf{F}}^p\mathbf{F}^{p^{-1}}\mathbf{F}^{e^{-1}} \tag{A.2}$$

where the elastic component is denoted by $\mathbf{L}^e = \dot{\mathbf{F}}^e\mathbf{F}^{e^{-1}}$ and $\widetilde{\mathbf{L}}^p = \dot{\mathbf{F}}^p\mathbf{F}^{p^{-1}}$ is the plastic component in $\widetilde{\mathcal{B}}$ which is linked to $\dot{\gamma}^\alpha$ i.e. the rate of slip.

$$\widetilde{\mathbf{L}}^p = \sum_\alpha \dot{\gamma}^\alpha \mathbf{m}_0^\alpha \otimes \mathbf{n}_0^\alpha \tag{A.3}$$

The subsequent development of the constitutive model and time-integration will be pertinent to the stress-free intermediate configuration whose non-uniqueness in the single crystal plasticity model is constitutively described by Eq. (A.3). $\mathbf{m}_0^\alpha$ and $\mathbf{n}_0^\alpha$, in the reference configuration, are the unit vectors of a slip system α denoting the slip direction and plane normal respectively [29, 32]. These unit vectors in the current configuration are obtained by the following equation.

$$\mathbf{m}^\alpha = \mathbf{F}^e\mathbf{m}_0^\alpha \quad \text{and} \quad \mathbf{n}^\alpha = \mathbf{n}_0^\alpha\mathbf{F}^{e^{-1}} \tag{A.4}$$

The unit vectors $\mathbf{m}_0^\alpha$ and $\mathbf{n}_0^\alpha$ are assumed orthogonal to each other. $\{111\}\langle110\rangle$ slip systems are favorable for the slip in face-centered cubic (FCC) materials. In configuration $\widetilde{\mathcal{B}}$, the elastic Green-Lagrange strain $\mathbf{E}^e$ is written as:

$$\mathbf{E}^e = \frac{1}{2}(\mathbf{F}^{e^T}\mathbf{F}^e - \mathbf{I}) \tag{A.5}$$

where the identity tensor is denoted by $\mathbf{I}$ which is of second-order. In $\widetilde{\mathcal{B}}$, the second Piola-Kirchhoff stress $\mathbf{T}^e$ relates to the Cauchy stress $\boldsymbol{\sigma}$ by the following equation.

$$\mathbf{T}^e = (\det\mathbf{F}^e)\mathbf{F}^{e^{-1}}\boldsymbol{\sigma}\mathbf{F}^{e^{-T}} \tag{A.6}$$

In the intermediate configuration $\widetilde{\mathcal{B}}$, a hyperelastic constitutive law is applied for defining the single crystal's stress–strain response. Using the Helmholtz potential energy of the lattice per unit volume ψ, the total stress–strain relationship is given below.

$$\mathbf{T}^e = \frac{\partial\psi}{\partial\mathbf{E}^e} \tag{A.7}$$

Differentiation of Eq. (A.7) with respect to $\mathbf{E}^e$ gives a fourth-order tensor κ.

$$\frac{\partial\mathbf{T}^e}{\partial\mathbf{E}^e} = \frac{\partial^2\psi}{\partial\mathbf{E}^{e^2}} = \kappa \tag{A.8}$$

The elastic deformation range in most of the crystalline materials, in comparison to the plastic strains, is infinitesimal. Thus, κ is approximated by anisotropic elasticity tensor $\mathbb{C}$ of the fourth-order to get the final constitutive law from Eq. (A.7).

$$\mathbf{T}^e = \mathbb{C} : \mathbf{E}^e \tag{A.9}$$

A.2 Kinetics

At a given temperature θ and shear stress τ_{th}^α, $\dot{\gamma}^\alpha$ is determined from the rate at which the lattice resistance is overcome by the dislocations. A dislocation starting its motion from the metastable equilibrium position towards another stable equilibrium configuration has to overcome the energetic path between the two configurations which is indicated by the activation energy or Gibbs free energy barrier i.e., ΔG. At a given temperature θ, the probability of energy

fluctuation allowing the dislocations to overcome this energy barrier is given in terms of the Boltzmann constant k_B from the theory of kinetics [55].

$$P_\theta^\alpha = \exp\left(-\frac{\Delta G}{k_B \theta}\right) \tag{A.10}$$

The slip (or plastic strain) rate arising due to the release of dislocations facing similar energy path barriers, at any instant, is given by:

$$\dot{\gamma}^\alpha = \dot{\gamma}_0 P_\theta^\alpha = \dot{\gamma}_0 \exp\left(-\frac{\Delta G}{k_B \theta}\right) \tag{A.11}$$

where the symbol $\dot{\gamma}_0$ denotes the slip rate's reference value. Using the expression proposed by Kocks et al. [30], the activation energy ΔG is expressed in terms of the Helmholtz free energy of activation, F_0, and the strength, $\hat{\tau}$, that dislocations must overcome without any aid of thermal activation.

$$\Delta G = F_0\left[1 - \left(\frac{\tau_{th}^\alpha}{\hat{\tau}}\right)^p\right]^q \tag{A.12}$$

Approximating the strength $\hat{\tau}$ by the product of $\hat{\tau}_o$ and $\frac{\mu}{\mu_0}$ i.e. the lattice friction stress at 0 K and shear moduli ratio respectively, the plastic shear strain rate becomes,

$$\dot{\gamma}^\alpha = \dot{\gamma}_0 \exp\left\{-\frac{F_0}{k_B \theta}\left[1 - \left(\frac{\tau_{th}^\alpha}{\hat{\tau}_o \frac{\mu}{\mu_0}}\right)^p\right]^q\right\} \tag{A.13}$$

where at temperatures θ and 0 K, the shear moduli of material are denoted by μ and μ_0 respectively. For only thermally and stress-activated lattice resistance, τ_{th}^α, i.e. the driving stress for activation energy in the above equation can be written in terms of the resolved shear stress τ^α and the athermal slip resistance τ_a^α,

$$\tau_{th}^\alpha = \tau^\alpha - \tau_a^\alpha \tag{A.14}$$

so that the final expression of the flow rate becomes,

$$\dot{\gamma}^\alpha = \dot{\gamma}_0 \exp\left[-\frac{F_0}{k_B \theta}\left\{1 - \left\langle\frac{|\tau^\alpha| - \tau_a^\alpha}{\hat{\tau}_o \frac{\mu}{\mu_0}}\right\rangle^p\right\}^q\right] sgn(\tau^\alpha) \tag{A.15}$$

where τ^α is defined as below.

$$\tau^\alpha = \mathbf{F}^{e^T}\mathbf{F}^e\mathbf{T}^e : \mathbf{m}_0^\alpha \otimes \mathbf{n}_0^\alpha \tag{A.16}$$

A.3 Time integration procedure

At time t_n, for the given state variables i.e. $\mathbf{F}_n^p$, $\mathbf{T}_n^e$, $\rho_{e,n}^\alpha$, $\rho_{s,n}^\alpha$, the corresponding updated state variables at the time t_{n+1} are found with an estimate of $\mathbf{F}_{n+1}$ over the time increment

$\Delta t = t_{n+1} - t_n$. Integrating the equation $\dot{\mathbf{F}}^p = \widetilde{\mathbf{L}}^p \mathbf{F}^p$ by the exponential operator, we get:

$$\mathbf{F}_{n+1}^p = \exp\left[\Delta t \widetilde{\mathbf{L}}_{n+1}^p\right]\mathbf{F}_n^p \tag{A.17}$$

Using the above with equation $\mathbf{F} = \mathbf{F}^e\mathbf{F}^p$, we get

$$\mathbf{F}_{n+1}^e = \mathbf{F}_{n+1}^{e,tr}\exp\left[-\Delta t \widetilde{\mathbf{L}}_{n+1}^p\right] \tag{A.18}$$

where $\mathbf{F}_{n+1}^{e,tr} = \mathbf{F}_{n+1}\mathbf{F}_n^{p-1}$ denotes the trial elastic deformation gradient tensor. The updated tensor of elastic strain can be obtained from the following.

$$\mathbf{E}_{n+1}^e = \frac{1}{2}(\mathbf{F}_{n+1}^{e^T}\mathbf{F}_n^e - \mathbf{I}) \tag{A.19}$$

Substituting the equations (A.17), (A.18) and (A.19) in the equation $\mathbf{T}^e = \mathbb{C} : \mathbf{E}^e$ and neglecting the higher-order terms, the stress update is obtained as:

$$\mathbf{T}_{n+1}^e = \mathbf{T}^{e,tr} - \sum_{\alpha=1}^{N} \Delta t \dot{\gamma}^\alpha \mathbf{C}^\alpha \tag{A.20}$$

where the terms $\mathbf{T}^{e,tr}$ and $\mathbf{C}^\alpha$ are given by

$$\mathbf{T}^{e,tr} = \mathbb{C}\left[\mathbf{E}_{n+1}^e\right] \tag{A.21}$$

$$\mathbf{C}^\alpha = \frac{1}{2}\mathbb{C} : \left[\mathbf{E}_{n+1}^e\left(\mathbf{m}_0^\alpha \otimes \mathbf{n}_0^\alpha\right) + \left(\mathbf{m}_0^\alpha \otimes \mathbf{n}_0^\alpha\right)^T\mathbf{E}_{n+1}^e\right]. \tag{A.22}$$

For the evolutionary equations of dislocation densities, the application of the Euler backward method yields the following equations.

$$\rho_{e,n+1}^\alpha = \rho_{e,n}^\alpha + \Delta t \dot{\rho}_{e,n+1}^\alpha \tag{A.23}$$

$$\rho_{s,n+1}^\alpha = \rho_{s,n}^\alpha + \Delta t \dot{\rho}_{s,n+1}^\alpha \tag{A.24}$$

The equations (A.20), (A.23) and (A.24) form a set of algebraic equations in state variables $\mathbf{T}_{n+1}^e$, $\rho_{e,n+1}^\alpha$ and $\rho_{s,n+1}^\alpha$ which are solved with Newton–Raphson method using a single iterative procedure. Recasting the above system of equations into the system of residuals yields

$$\begin{bmatrix} r_{\mathbf{T}^e} \\ r_{\rho_e^\alpha} \\ r_{\rho_s^\alpha} \end{bmatrix} = \begin{bmatrix} \mathbf{T}_{n+1}^e - \left(\mathbf{T}^{e,tr} - \sum_{\alpha=1}^{N}\Delta t \dot{\gamma}^\alpha \mathbf{C}^\alpha\right) \\ \rho_{e,n+1}^\alpha - \left(\rho_{e,n}^\alpha + \Delta t \dot{\rho}_{e,n+1}^\alpha\right) \\ \rho_{s,n+1}^\alpha - \left(\rho_{s,n}^\alpha + \Delta t \dot{\rho}_{s,n+1}^\alpha\right) \end{bmatrix} \tag{A.25}$$

Linearisation of equation (A.25) gives

$$\begin{bmatrix} \frac{\partial r_{\mathbf{T}^e}}{\partial \mathbf{T}^e} & \frac{\partial r_{\mathbf{T}^e}}{\partial \rho_e^\beta} & \frac{\partial r_{\mathbf{T}^e}}{\partial \rho_s^\beta} \\ \frac{\partial r_{\rho_e^\alpha}}{\partial \mathbf{T}^e} & \frac{\partial r_{\rho_e^\alpha}}{\partial \rho_e^\beta} & \frac{\partial r_{\rho_e^\alpha}}{\partial \rho_s^\beta} \\ \frac{\partial r_{\rho_s^\alpha}}{\partial \mathbf{T}^e} & \frac{\partial r_{\rho_s^\alpha}}{\partial \rho_e^\beta} & \frac{\partial r_{\rho_s^\alpha}}{\partial \rho_s^\beta} \end{bmatrix}^{(i)}_{n+1} \begin{bmatrix} \delta \mathbf{T}^e \\ \delta \rho_e^\alpha \\ \delta \rho_s^\alpha \end{bmatrix}^{(i+1)}_{(n+1)} = - \begin{bmatrix} r_{\mathbf{T}^e} \\ r_{\rho_e^\alpha} \\ r_{\rho_s^\alpha} \end{bmatrix}^{(i)}_{(n+1)} \tag{A.26}$$

The solution variables at $(i+1)^{th}$ iteration of the iterative procedure are updated as

$$\mathbf{T}^{e(i+1)}_{n+1} \leftarrow \mathbf{T}^{e(i)}_n + \delta \mathbf{T}^{e(i+1)}_{n+1} \tag{A.27}$$

$$\rho^{\alpha(i+1)}_{e,n+1} \leftarrow \rho^{\alpha(i)}_{e,n} + \delta \rho^{\alpha(i+1)}_{e,n+1} \tag{A.28}$$

$$\rho^{\alpha(i+1)}_{s,n+1} \leftarrow \rho^{\alpha(i)}_{s,n} + \delta \rho^{\alpha(i+1)}_{s,n+1} \tag{A.29}$$

For a time instant t_{n+1}, the above iterative procedure continues until the convergence of the solution is achieved i.e. Equation (A.26) is satisfied within the necessary tolerance. The incremental vector's norm is employed as the basis for the stopping criterion in this work:

$$\|\delta \mathbf{T}^{e(i+1)}_{n+1}\| + \|\delta S^{\alpha(i+1)}_{n+1}\| < e \tag{A.30}$$

where S denotes the slip resistance and the defined tolerance for controlling the accuracy of the aforementioned convergence criterion is $e = 0.1$. Whereas, to maintain the stability of the criterion, a maximum allowable tolerance $e_{max} = 1.0$ is used in this work.

Since there is no guarantee of plastic incompressibility, the state variables are updated using the plastic deformation gradient normalized as below.

$$\mathbf{F}^p_{n+1} \leftarrow \left[\det\left(\mathbf{F}^p_{n+1} \right) \right]^{\frac{-1}{3}} \mathbf{F}^p_{n+1} \tag{A.31}$$

At last, the updated Cauchy stress $\boldsymbol{\sigma}_{n+1}$ is calculated as

$$\boldsymbol{\sigma}_{n+1} = (\det \mathbf{F}^e)^{-1}_{n+1} \mathbf{F}^e_{n+1} \mathbf{T}^e_{n+1} \mathbf{F}^{e^T}_{n+1}. \tag{A.32}$$

A.4 Periodic boundary conditions

The RVE's deformation is mapped through a homogenized deformation gradient $\overline{\mathbf{F}}$ by:

$$\mathbf{y} = \overline{\mathbf{F}} \mathbf{x} + \widetilde{\mathbf{w}} \tag{A.33}$$

where the position vectors $\mathbf{x}$ and $\mathbf{y}$ stand for the original and current configurations of a material point respectively. The fluctuation field brought on by the heterogeneous microstructure is represented by $\widetilde{\mathbf{w}}$. Differentiating Eq. (A.33) partially w.r.t $\mathbf{x}$,

$$\frac{\partial \mathbf{y}}{\partial \mathbf{x}} = \overline{\mathbf{F}} + \frac{\partial \widetilde{\mathbf{w}}}{\partial \mathbf{x}} \tag{A.34}$$

and using the definition $\mathbf{F} = \frac{\partial \mathbf{y}}{\partial \mathbf{x}}$, we get:

$$\mathbf{F} = \overline{\mathbf{F}} + \widetilde{\mathbf{F}} \tag{A.35}$$

where $\widetilde{\mathbf{F}}$ is the fluctuating deformation gradient. The displacement field $\mathbf{u}$ can also be split into homogenized and fluctuating parts i.e. $\overline{\mathbf{u}}$ and $\widetilde{\mathbf{u}}$.

$$\mathbf{u} = (\overline{\mathbf{F}} - \mathbf{I})\mathbf{x} + \widetilde{\mathbf{u}} = \overline{\mathbf{u}} + \widetilde{\mathbf{u}} \tag{A.36}$$

By volume averaging $\mathbf{F}$, the homogenized deformation gradient, denoted by $\overline{\mathbf{F}}$, is determined as below.

$$\overline{\mathbf{F}} = \frac{1}{V} \int \mathbf{F} dV \tag{A.37}$$

Substitution of $\mathbf{F}$ from Eq. (A.35) yields,

$$\overline{\mathbf{F}} = \frac{1}{V} \int (\overline{\mathbf{F}} + \widetilde{\mathbf{F}}) dV = \overline{\mathbf{F}} + \frac{1}{V} \int \widetilde{\mathbf{F}} dV, \tag{A.38}$$

or

$$\frac{1}{V} \int \widetilde{\mathbf{F}} dV = 0. \tag{A.39}$$

This implies

$$\int \widetilde{\mathbf{F}} dV = \int_{\partial S} \widetilde{\mathbf{w}} \otimes \mathbf{n} dS = \int_{\partial S^+} \widetilde{\mathbf{w}}^+ \otimes \mathbf{n}^+ dS + \int_{\partial S^-} \widetilde{\mathbf{w}}^- \otimes \mathbf{n}^- dS = 0 \tag{A.40}$$

where $\mathbf{n}^+$ and $\mathbf{n}^-$ denote the normals outward to the opposing surfaces (∂S^+ and ∂S^-). Therefore, according to Eq. (A.40), when $\widetilde{\mathbf{w}}^+ = \widetilde{\mathbf{w}}^-$, the periodicity boundary condition is achieved.

Data availability Not available.

Declarations

Conflict of interest All authors declare that they have no conflicts of interest.

Ethical approval This article does not contain any studies with human participants or animals performed by any of the authors.

References

1. Dursun T, Soutis C. Recent developments in advanced aircraft aluminium alloys. Mater Design. 2014;56:862–71.
2. Andersen SJ, Marioara CD, Friis J, Wenner S, Holmestad R. Precipitates in aluminium alloys. Adv Phys: X. 2018;3(1):1479984.
3. Zhu L, Li N, Childs P. Light-weighting in aerospace component and system design. Propuls Power Res. 2018;7(2):103–19.

4. Argon A. Strengthening mechanisms in crystal plasticity, OUP Oxford, 2007.

5. Sehitoglu H, Foglesong T, Maier H. Precipitate effects on the mechanical behavior of aluminum copper alloys part i. experiments,. Metall Mater Trans A. 2005;36(3):749–61.

6. Esin VA, Briez L, Sennour M, Köster A, Gratiot E, Crépin J. Precipitation-hardness map for Al-Cu-Mg alloy (AA2024-T3). J Alloys Compd. 2021;854:157164.

7. Garcia-Hernandez J, Garay-Reyes C, Gomez-Barraza I. Influence of plastic deformation and cu/mg ratio on the strengthening mechanisms and precipitation behavior of AA2024 aluminum alloys. J Mater Res Technol. 2019;8(6):5471–5.

8. Sehitoglu H, Foglesong T, Maier H. Precipitate effects on the mechanical behavior of aluminum copper alloys Part ii modeling. Metall Mater Trans A. 2005;36(13):763–70.

9. Lebensohn RA, Tomé C. A self-consistent anisotropic approach for the simulation of plastic deformation and texture development of polycrystals: application to zirconium alloys. Metall Mater Trans A. 1993;41(9):2611–24.

10. Acharya A, Beaudoin A. Grain-size effect in viscoplastic polycrystals at moderate strains. J Mech Phys Solids. 2000;48(10):2213–30.

11. Bhattacharyya J, Bittmann B, Agnew S. The effect of precipitate-induced backstresses on plastic anisotropy: Demonstrated by modeling the behavior of aluminum alloy, 7085. Int J Plast. 2019;117:3–20.

12. Turner P, Tomé C. A study of residual stresses in zircaloy-2 with rod texture. Acta Metall Mater. 1994;42(12):4143–53.

13. Anjabin N, Taheri AK, Kim H. Crystal plasticity modeling of the effect of precipitate states on the work hardening and plastic anisotropy in an Al-Mg-Si alloy. Comput Mater Sci. 2014;83:78–85.

14. Myhr O, Grong Ø, Andersen S. Modelling of the age hardening behaviour of Al-Mg-Si alloys. Acta Mater. 2001;49(1):65–75.

15. Gouttebroze S, Mo A, Grong Ø, Pedersen K, Fjær H. A new constitutive model for the finite element simulation of local hot forming of aluminum 6xxx alloys. Metall and Mater Trans A. 2008;39(3):522–34.

16. Kocks U, Mecking H. Physics and phenomenology of strain hardening: the fcc case. Prog Mater Sci. 2003;48(3):171–273.

17. Estrin Y, Mecking H. A unified phenomenological description of work hardening and creep based on one-parameter models. Acta Metall. 1984;32(1):57–70.

18. Li YL, Kohar CP, Mishra RK, Inal K. A new crystal plasticity constitutive model for simulating precipitation-hardenable aluminum alloys. Int J Plast. 2020;132:102759.

19. Esmaeili S, Lloyd D. Modeling of precipitation hardening in pre-aged AlMgSi (Cu) alloys. Acta Mater. 2005;53(20):5257–71.

20. Molinari A, Ahzi S, Kouddane R. On the self-consistent modeling of elastic-plastic behavior of polycrystals. Mech Mater. 1997;26(1):43–62.

21. Li YL, Kohar CP, Muhammad W, Inal K. Precipitation kinetics and crystal plasticity modeling of artificially aged AA6061. Int J Plast. 2022;152:103241.

22. Bardel D, Perez M, Nelias D, Deschamps A, Hutchinson CR, Maisonnette D, Chaise T, Garnier J, Bourlier F. Coupled precipitation and yield strength modelling for non-isothermal treatments of a 6061 aluminium alloy. Acta Mater. 2014;62:129–40.

23. Peirce D, Asaro RJ, Needleman A. Material rate dependence and localized deformation in crystalline solids. Acta Metall. 1983;31(12):1951–76.

24. Li L, Shen L, Proust G, Loo Chin Moy C, Ranzi G, A crystal plasticity representative volume element model for simulating nanoindentation of aluminium alloy 2024, ICCM2012 Proceedings (2012).

25. Li L, Shen L, Proust G, Moy CK, Ranzi G. Three-dimensional crystal plasticity finite element simulation of nanoindentation on aluminium alloy 2024. Mater Sci Eng, A. 2013;579:41–9.

26. Efthymiadis P, Pinna C, Yates JR. Fatigue crack initiation in AA2024: a coupled micromechanical testing and crystal plasticity study. Fatigue Fract Eng Mater Struct. 2019;42(1):321–38.

27. Toursangsaraki M, Wang H, Hu Y, Karthik D. Crystal plasticity modeling of laser peening effects on tensile and high cycle fatigue properties of 2024–T351 aluminum alloy. J Manuf Sci Eng. 2021;143(7):1–24.

28. Aghabalaeivahid A, Shalvandi M. Microstructure-based crystal plasticity modeling of AA2024-T3 aluminum alloy defined as the α-al, θ-Al2Cu, and S-Al2CuMg phases based on real metallographic image. Mater Res Express. 2021;8(10):106521.

29. Peirce D, Asaro R, Needleman A. An analysis of nonuniform and localized deformation in ductile single crystals. Acta Metall. 1982;30(6):1087–119.

30. Kocks U, Argon A, Ashby M Thermodynamics and kinetics of slip, 1975, Progress in Materials Science 19.

31. Cheong K-S, Busso EP. Discrete dislocation density modelling of single phase fcc polycrystal aggregates. Acta Mater. 2004;52(19):5665–75.

32. Alankar A, Mastorakos IN, Field DP. A dislocation-density-based 3d crystal plasticity model for pure aluminum. Acta Mater. 2009;57(19):5936–46.

33. Rodríguez-Martínez JA, Rusinek A, Arias A. Thermo-viscoplastic behaviour of 2024–T3 aluminium sheets subjected to low velocity perforation at different temperatures. Thin-Walled Struct. 2011;49(7):819–32.

34. Khan I, Starink MJ. A multi-mechanistic model for precipitation strengthening in Al-Cu-Mg alloys during non-isothermal heat treatments. Mater Sci Forum. 2006;519:277–82.

35. Bardel D, Perez M, Nelias S, Dancette S, Chaudet P, Massardier V. Cyclic behaviour of a 6061 aluminium alloy: Coupling precipitation and elastoplastic modelling. Acta Mater. 2015;83:256–68.

36. Segurado J, Llorca J. Simulation of the deformation of polycrystalline nanostructured ti by computational homogenization. Comput Mater Sci. 2013;76:3–11.

37. Abd El-Aty A, Xu Y, Ha S, Zhang S-H. Computational homogenization of tensile deformation behaviors of a third generation Al-Li alloy 2060–T8 using crystal plasticity finite element method. Mater Sci Eng A. 2018;731:583–94.

38. Li J, Romero I, Segurado J. Development of a thermo-mechanically coupled crystal plasticity modeling framework: application to polycrystalline homogenization. Int J Plast. 2019;119:313–30.

39. Huet C. Application of variational concepts to size effects in elastic heterogeneous bodies. J Mech Phys Solids. 1990;38(6):813–41.

40. Hazanov S, Huet C. Order relationships for boundary conditions effect in heterogeneous bodies smaller than the representative volume. J Mech Phys Solids. 1994;42(12):1995–2011.

41. Segurado J, Llorca J. A numerical approximation to the elastic properties of sphere-reinforced composites. J Mech Phys Solids. 2002;50(10):2107–21.

42. Singh L, Ha S, Vohra S, Sharma M. Computational homogenization based crystal plasticity investigation of deformation behavior of AA2024-T3 alloy at different strain rates. Multidiscip Model Mater Struct. 2023;19(3):420–40.

43. Ritz H, Dawson P. Sensitivity to grain discretization of the simulated crystal stress distributions in fcc polycrystals. Modell Simul Mater Sci Eng. 2008;17(1):015001.

44. Knezevic M, Drach B, Ardeljan M, Beyerlein IJ. Three dimensional predictions of grain scale plasticity and grain boundaries using crystal plasticity finite element models. Comput Methods Appl Mech Eng. 2014;277:239–59.

45. Feather WG, Lim H, Knezevic M. A numerical study into element type and mesh resolution for crystal plasticity finite

element modeling of explicit grain structures. Comput Mech. 2021;67(1):33–55.

46. Quey R, Dawson P, Barbe F. Large-scale 3d random polycrystals for the finite element method: Generation, meshing and remeshing. Comput Methods Appl Mech Eng. 2011;200(17–20):1729–45.

47. Agaram S, Kanjarla AK, Bhuvaraghan B, Srinivasan SM. Dislocation density based crystal plasticity model incorporating the effect of precipitates in IN718 under monotonic and cyclic deformation. Int J Plast. 2021;141:102990.

48. Beausir B, Fundenberger J, Analysis tools for electron and x-ray diffraction, atex-software; université de lorraine-metz. 2017, Available online: www. atex-software. eu.

49. Quey R, Kasemer M. The neper/fepx project: free/open-source polycrystal generation, deformation simulation, and post-processing. IOP Conference Series: Mat Sci Eng. 2022;1249:012021

50. Ha S, Jang J-H, Kim K. Finite element implementation of dislocation-density-based crystal plasticity model and its application to pure aluminum crystalline materials. Int J Mech Sci. 2017;120:249–62.

51. Balasubramanian S, Anand L. Elasto-viscoplastic constitutive equations for polycrystalline fcc materials at low homologous temperatures. J Mech Phys Solids. 2002;50(1):101–26.

52. Liu G, Zhang G, Ding X, Sun J, Chen K. The influences of multi-scale-sized second-phase particles on ductility of aged aluminum alloys. Metall Mater Trans A. 2004;35(6):1725–34.

53. Bandyopadhyay R, Prithivirajan V, Sangid MD. Uncertainty quantification in the mechanical response of crystal plasticity simulations. JOM. 2019;71(8):2612–24.

54. Asaro RJ. Crystal plasticity. ASME J Appl Mech. 1983;50(4b):921–34.

55. E. P. Busso. Cyclic deformation of monocrystalline nickel aluminide and high temperature coatings, Ph.D. thesis, Massachusetts Institute of Technology. 1990.